

Oceanic kinetic energy in the spectral space and role of wind power in the Kuroshio-Oyashio extension

Mingkui Li¹ · Haiyuan Yang^{1,2} · Jinzhuo Cai¹ · Zhaohui Chen^{1,2} · Lixin Wu^{1,3}

Received: 13 March 2025 / Accepted: 17 September 2025 / Published online: 29 September 2025 © Springer-Verlag GmbH Germany, part of Springer Nature 2025

Abstract

Using the high-resolution outputs from the Coupled Regional Climate Model (CRCM), this study investigates the kinetic energy budget and the role of wind power in the Kuroshio-Oyashio Extension (KOE) region. CRCM reproduces key features of the KOE circulation system, including the oceanic current, eddy activity, and wind patterns. Energy budget analysis reveals a balance between vertical mixing and pressure work as the main regulators of kinetic energy, with non-linear effects and horizontal mixing playing a secondary role. Furthermore, the study identifies a peak of kinetic energy at 250 km, and an inverse energy cascade with energy flux from small to large scales. Wind power analysis shows that it injects energy into the ocean at large scales and extracts energy at mesoscale and smaller scales, influencing vertical mixing. Work of time-mean wind stress on circulation fluctuations potentially regulating the energy cascade. This study provides insights into the kinetic energy in spectrum and role of wind power of the KOE region.

Keywords Kuroshio-Oyashio extension · Kinetic energy balance · Energy cascade · Wind power

1 Introduction

The Kuroshio-Oyashio Extension (KOE) is located in the North Pacific Ocean, where the warm Kuroshio meets the cold Oyashio (Fig. 1; Yasuda 2003; Kelly et al. 2010; Qiu 2019). The Kuroshio Extension originates from the Kuroshio which transports a large amount of warm and saline water from the Indo-Pacific warm pool, reaching a speed of up to 1–2 m s⁻¹ (Qiu et al. 1991; 2019; Jayne et al. 2009; Hu et al. 2015). Fed by the large available potential energy stored in the strong current, energetic meanders are periodically generated and eddies are frequently pinched off from the jet, making this area the most

Responsible Editor Akira Nagano.

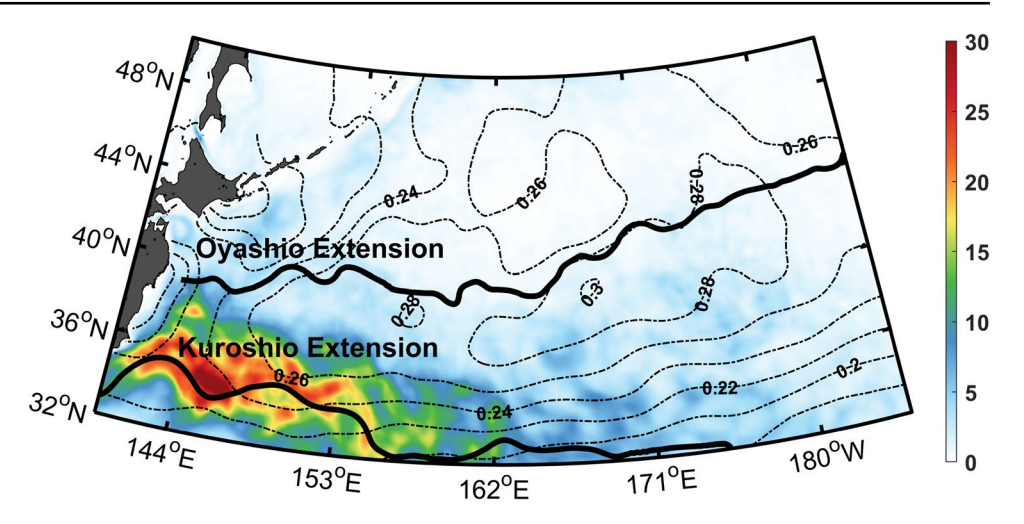
- Haiyuan Yang yanghaiyuan@ouc.edu.cn
- Frontier Science Center for Deep Ocean Multispheres and Earth System (FDOMES), Physical Oceanography Laboratory, Ocean University of China, Qingdao, China
- ² Laboratory for Ocean Dynamics and Climate, Qingdao Marine Science and Technology Center, Qingdao, China
- ³ Laoshan Laboratory, Qingdao, China

eddy-rich region in the global ocean (Qiu and Chen 2005; 2010; Waterman et al. 2011; Chen et al. 2014, 2016; Yang et al. 2017, 2018; Ji et al. 2018). The Oyashio Extension is formed after the Oyashio separated from the western boundary around 40°N. It brings cold, fresh water from the subpolar region (Wu et al. 2018; 2019; Qiu 2019). Compared with the Kuroshio Extension characterized by intense oceanic current and eddies, the Oyashio Extension presents a relatively weaker transport but stronger temperature variability (Nakamura and Miyama 2014; Kida et al. 2016; Jing et al. 2019; Cai et al. 2024). When the warm Kuroshio water meets the cold Oyashio water in the KOE region, it forms a strong frontal zone. The fronts can be tens of kilometers wide with large cross-front temperature differences (Qu et al. 2001; Kida et al. 2016; Wu et al. 2018; 2019; Nishikawa et al. 2020; Zhou and Cheng 2022). The intense currents, vigorous eddy activity, and strong fronts in the KOE region dynamically interact, rendering it one of the most complex circulation systems in the global oceans, characterized by intense multiscale interactions and cross-scale energy transfer.

The interaction between different processes in the KOE region can be described by the energy flux among different scales, i.e., energy cascade. Based on observation studies, mesoscale processes draw energy from the mean flow



Fig. 1 The KOE region. Shading shows the averaged sea surface eddy kinetic energy (EKE; Unit: 0.01 m² s⁻²) during October—March of 2004–2008 from FORA-WNP30 product. Thick black lines show the positions of the Kuroshio Extension and the Oyashio Extension axes, which are defined as sea surface height contours of 0.25 m and −0.5 m, respectively. Dashed contours show the climatology mean wind stress (Unit: N m⁻²) during 2004–2008 from QuikSCAT satellite observation



through baroclinic and barotropic instabilities (Qiu and Chen 2005; Chelton et al. 2011; Qiu et al. 2022), and are the major contributors of kinetic energy in the KOE region which accounts for more than 70% of the total value (Qiu et al. 1991; Hurlburt et al. 1996; Scharffenberg and Stammer 2010). Therefore, the studies of energy cascades unfold with a focus on mesoscale processes. Historically, the prevailing theory suggested that energy inversely cascades from mesoscale eddies to large scale circulation (Arbic and Flierl 2004; Scott and Wang 2005; Schlösser & Eden 2007; Qiu et al. 2008; Aluie et al. 2018). Recently, studies using very high-resolution ocean modeling and observational techniques revealed the importance of small-scale processes, such as submesoscale processes, in the overall energy budget of the KOE region (Siegelman et al. 2020; Dong et al. 2022; Wang et al. 2022; Yang et al. 2024; Zhu et al. 2024). These submesoscale processes are generated from several classes of surface frontal instabilities such as frontogenesis, mixed layer instability and turbulent thermal wind (Boccaletti et al. 2007; Fox-Kemper et al. 2008; Thomas et al. 2013; Gula et al. 2014; McWilliams 2016; Dauhajre and McWilliams 2018; McWilliams et al. 2019; Taylor and Thompson 2023). During their generation, potential energy stored in the intense front and/or mixed larger is released to submesoscale motions. Correspondingly, a robust bi-directional transfer of kinetic energy with respect to submesoscale in the upper ocean is proved (Scott and Wang 2005; Aluie et al. 2018; Qiu et al. 2022). Inverse cascades, characterized by energy transfer from submesoscale to mesoscale and then larger scales, predominate at longer wavelengths. Conversely, forward cascades, where energy moves from submesoscale to smaller scales, are prevalent at shorter wavelengths. This perspective highlights the intricate interplay of different scales in ocean dynamics. However, in the KOE region, where multi-scale ocean dynamic interactions are prominent, the characteristics of the kinetic energy distribution and cascade in spectral space based on total kinetic

energy (Chen et al. 2015), rather than just eddy kinetic energy (EKE), remain unexamined.

Besides the complex oceanic processes, KOE is also a region of multi-scale air-sea interaction in global ocean, which is crucial for mid-latitude climate (Stommel 1979; Sprintall et al. 1995; Rhines et al. 2008; Hu et al. 2015). The substantial temperature difference between the warm Kuroshio water and the cold Oyashio water creates strong baroclinic zones. These zones are key in influencing overlying atmospheric circulation and variability (Hoskins and Valdes 1990; Nonaka et al. 2009; Hogg et al. 2009; Kaspi and Schneider 2013; Nakayama et al. 2021). For instance, they have a major impact on the position and intensity of the jet stream and storm (Hoskins and Valdes 1990; Nakamura and Shimpo 2004; Seo et al. 2023). The jet stream and storm, in turn, play a crucial role in shaping the wind field in the North Pacific, which regulates the states of KOE. At the oceanic mesoscale, meanders and eddies are the important dynamic elements that actively participate in the exchange of heat, momentum, and other properties between the ocean and the atmosphere (Chelton et al. 2001; 2004; Xie 2004; Kelly et al. 2010). On one hand, the heat and moisture vented by meanders and eddies, especially the warm-core ones, are thought to be indispensable in shaping the storm track, cloud formation and precipitation (Small et al. 2008; Ma et al. 2016; Liu et al. 2018; Seo et al. 2023). On the other hand, atmosphere damps the oceanic mesoscale processes by drawing heat (Guo and Bishop 2022; Guo et al. 2022; Shan et al. 2020; Yang et al. 2019, 2021; Renault et al. 2023) and doing negative work on current (Eden and Dietze 2009; Gaube et al. 2015; Renault et al. 2017, 2019; Seo et al. 2015; Seo 2017; Zhai et al. 2012), regulating eddy activity level and even affecting the large-scale circulation (Ma et al. 2016). However, a critical oversight in previous energy cascade studies is the lack of consideration for the impact of ocean-atmosphere interactions on the oceanic energy cascade, an area warranting further investigation. This nuanced



understanding underscores the complexity of oceanic energy dynamics and the need for comprehensive models that incorporate both oceanic and atmospheric influences.

To address the aforementioned issues, this study employs output from an ocean-mesoscale-eddy-resolving model. Given that our model cannot resolve submesoscale and smaller processes, we focus specifically on mesoscale and larger-scale dynamics. Here, we will explore the kinetic energy distribution and cascade in spectral space, and clarify the role of wind power in modulating them. The rest of this paper is organized as follows: Sect. 2 provides a brief introduction to the model settings and methodology used in this study. Section 3 first presents the kinetic energy distribution and energy cascade, and then details the role of wind power in eddy energetics based on the spectral energy budget. This paper ends with a conclusion and a brief discussion in Sect. 4.

2 Data and method

2.1 CRCM model

In this study, the effect of wind power on oceanic kinetic energy is estimated based on the outputs from the Coupled Regional Climate Model (CRCM). CRCM is originally developed at Texas A&M University with the aim of investigating the climate system in the North Pacific Ocean region. A detailed model description is provided by Ma et al. (2016). Here we briefly describe its atmospheric component – the Weather Research and Forecasting Model (WRF; Skamarock et al. 2008) and its oceanic component - the Regional Ocean Modelling Systems (ROMS). WRF is divided into 30 vertical levels with RRTMG and Goddard scheme for longwave and shortwave radiation (Mlawer et al. 1997; Chou and Suarez 1994), Lin et al.'s (1983) scheme for microphysics, Smagorinsky scheme for calculating eddy coefficient (Smagorinsky 1963), Hong and Pan's (1996) scheme for planetary boundary layer, Kain-Fritsch scheme for cumulus parameterization (Kain 2004), and Noah scheme for land surface. ROMS has 50 levels in a vertical terrain-following coordinate. The K-profile parameterization turbulent mixing closure scheme (Large et al. 1994) for vertical mixing and a bi-harmonic horizontal Smagorinsky-like mixing for momentum (Griffies and Hallberg 2000) are applied. CRCM consists of a comprehensive coupling software framework that allows frequent mass, momentum and energy exchanges at the air-sea interface every hour. WRF provides heat, freshwater flux, and wind stress to ROMS, while receiving SST and surface current velocity from ROMS. Compared to traditional ocean circulation models, the coupled model enables the atmosphere adjustment based on changes in ocean temperature and circulation. This leads to a better simulation of air-sea exchange and consequently allows for a more accurate assessment of atmospheric influences on oceanic dynamic processes.

The model is configured closely following Ma et al. (2016), with a common Arakawa-C grid shared by ROMS and WRF at 9-km horizontal resolution extending from 3.6°N to 66°N and from 99°E to 270°E to cover the entire North Pacific Ocean. To focus on the boreal winter when the atmospheric activity is energetic, the simulation is initialized on 1 October 2006 and runs for six months with the same initial and lateral boundary conditions as Ma et al. (2016). Daily averaged ocean variables as well as diagnostic terms for momentum equations within the domain (140°E-170°E, 32°N-46°N) are used.

2.2 FORA-WNP30 products

To validate the CRCM simulation, Four-dimensional variational Ocean Re-Analysis for the Western North Pacific over 30 years (FORA-WNP30) product (http://synthesis. jamstec.go.jp/FORA/e/; Usui et al. 2017) is used. It is based on the western North Pacific version of the Meteorological Research Institute (MRI) Community Ocean Model version 2.4 (MRI.COM-WNP; Tsujino et al. 2006). The horizontal resolution of this model is not constant: it is 1/10° within 117°E-160°E and 1/6° in 160°E-160°W zonally, while 1/10° within 15°N-50°N and 1/6° in 50°N-65°N in the meridional direction. In the vertical direction, there are 54 levels. A biharmonic operator is used in the horizontal mixing and friction, while the vertical viscosity and diffusivity are determined in accordance with Noh and Jin Kim (1999). MRI. COM-WNP is driven by the atmospheric forcing derived from the Japanese 55-year Reanalysis (JRA-55; Kobayashi et al. 2015). With the application of the MRI Multivariate Ocean Variational Estimation system (MOVE-4DVAR), the model assimilates several available in situ and satellite observations (e.g., in situ temperature and salinity profiles, SST, and SSH). Because of its good performance, FORA-WNP30 has been used to explore multiscale oceanic dynamics in the North Pacific region (Jing et al. 2019; Wang and Pierini 2020; Long et al. 2021; Yang et al. 2023). In this paper, daily mean data in the region (140°E-175°W, 32°N-50°N) during 2004-2008 are used.

2.3 Satellite observations

In addition to FORA-WNP30, wind stress data provided by SeaWinds scatterometer on the QuikSCAT satellite are also used to validate the CRCM. The SeaWinds scatterometer



87 Page 4 of 13 Ocean Dynamics (2025) 75:87

wind retrievals are accurate to better than 2 m s⁻¹ in speed and 20° in direction, with performance comparable to in-situ point measurements from buoys (Chelton et al. 2004). Here, we use the daily averaged QuikSCAT data on a $0.25^{\circ} \times 0.25^{\circ}$ grid in the region ($140^{\circ}\text{E}-175^{\circ}\text{W}$, $32^{\circ}\text{N}-50^{\circ}\text{N}$) during 2004-2008.

2.4 Kinetic energy budget

To reveal processes shaping the kinetic energy in the upper ocean and their potential regulation by wind power input, a budget analysis is conducted. The kinetic energy balance in physical space is as follows:

$$\underbrace{\rho_0 \frac{\partial}{\partial t} (\frac{1}{2} \boldsymbol{u}_h \cdot \boldsymbol{u}_h)}_{TEND_K} = \underbrace{-\rho_0 (\boldsymbol{u} \cdot \nabla) \, \boldsymbol{u}_h \cdot \boldsymbol{u}_h}_{NONL_K} - \underbrace{\nabla_h p \cdot \boldsymbol{u}_h}_{P_K} + \underbrace{\rho_0 \boldsymbol{D}_H \cdot \boldsymbol{u}_h}_{D_{HK}} + \underbrace{\rho_0 \boldsymbol{D}_V \cdot \boldsymbol{u}_h}_{D_{VK}}$$
(1)

Here, $\mathbf{u} = (u,v,w)$ and $\mathbf{u}_h = (u,v)$ are the three-dimensional velocity and its horizontal component, $\mathbf{D}_H = (D_{uh}, D_{vh})$ and $\mathbf{D}_V = (D_{uv}, D_{vv})$ the horizontal and vertical mixing terms, p the hydrostatic pressure, f Coriolis parameter, and ρ represents the density with its reference value ρ_0 set to be 1027.5 kg m⁻³. ∇ denotes the divergence operator. To get a better understanding of the energy distribution in different length scales, the kinetic energy budget in wavenumber space is also analyzed:

$$\underbrace{\frac{\rho_0 \frac{\partial}{\partial t} \mathcal{R}(\frac{1}{2} \widehat{\boldsymbol{u}_h} \cdot \widehat{\boldsymbol{u}_h}^*)}_{TEND_K} =}_{TEND_K} = \underbrace{\mathcal{R}\left(-\rho_0 \left(\widehat{\boldsymbol{u}} \cdot \widehat{\nabla}\right) \boldsymbol{u}_h \cdot \widehat{\boldsymbol{u}_h}^*\right) + \mathcal{R}\left(-\widehat{\nabla}_h \widehat{\boldsymbol{p}} \cdot \widehat{\boldsymbol{u}_h}^*\right) +}_{P_K} + \underbrace{\mathcal{R}\left(\rho_0 \widehat{\boldsymbol{D}_V} \cdot \widehat{\boldsymbol{u}_h}^*\right)}_{D_{VK}} + \underbrace{\mathcal{R}\left(\rho_0 \widehat{\boldsymbol{D}_V} \cdot \widehat{\boldsymbol{u}_h}^*\right)}_{D_{VK}}, \tag{2}$$

where the caret denotes the two-dimensional Fourier transform, star denotes the complex conjugate, and R is the real part operator. To calculate the terms in Eq. 2, a two-dimensional Fourier decomposition is implanted onto four overlapping subdomains with 128×128 grid points ($12.8^{\circ} \times 12.8^{\circ}$), centered at 40.9°N, and every 2° longitude from 157.8°E to 163.8°E (please refer to the grey boxes in Fig. 2b). The boxes are positioned far from the Japanese archipelago to minimize land effects. Moreover, it is found that the selected region primarily covers the northern flank of the KE. The primary reason for this selection is that the KE itself features intense currents inducing strong advective effects. Although this does not substantially alter the energy budget, it compromises the accuracy of cross-scale interaction assessments within the nonlinear terms (please refer to the discussion of $\Pi(K)$ in Section 3.2). For each box and each

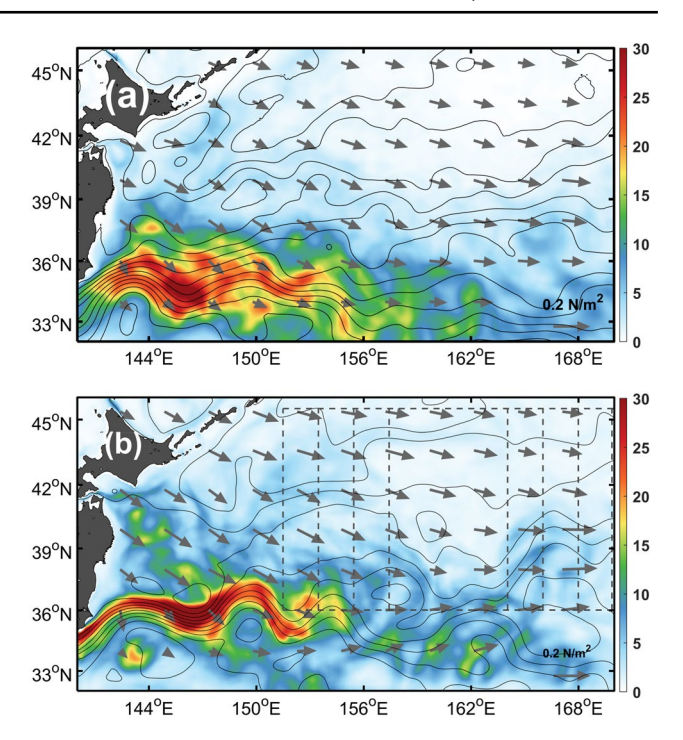


Fig. 2 Comparison of FORA/QuikSCAT data and CRCM output during October–March. **a** Shading and thin black contours show the averaged EKE (Unit: 0.01 m² s⁻²) and SSH (Unit: m; Interval: 0.1 m) from FORA-WNP30 product, while the overlying gray arrows show the wind field during the same period from QuikSCAT satellite observation. **b** is similar to (**a**) but using EKE, SSH and wind field from the CRCM model. Dashed boxes denote the budget analysis region

time step, the associated variables are first detrended by fitting a bilinear plane via least squares. A Hanning window is then applied to the detrended data before the Fourier transform (Qiu et al. 2008; Wang et al. 2019). In Eqs. 1 and 2, the term on the left-hand side corresponds to the tendency of the kinetic energy (denoted as TEND_K), which is controlled by the production and destruction processes shown on the right-hand side of the equation. On the right-hand side, the NONL_K term describes the joint effects of the redistribution of kinetic energy among different wavenumbers through the nonlinear interaction and the transport of energy in or out of the domain through the boundaries. The integral of the former over all the wavenumbers is zero, whereas the integral of the latter is not. This term provides a vital tool for understanding cross-scale energy transfer in this region and will be examined in detail in the subsequent discussion. The P_K term denotes the evolution of kinetic energy associated with work done by horizontal pressure gradient (pressure work hereinafter), whereas D_{HK} and D_{VK} are respectively horizontal and vertical mixing processes.

In the CRCM, wind stress, i.e. $\tau = (\tau_x, \tau_y)$, is involved in the boundary conditions of D_{V} . Its effect on oceanic kinetic energy balance is estimated by WP, which is defined as the product of τ and sea surface geostrophic flow \mathbf{u}_{geo} :



$$WP = \boldsymbol{\tau} \cdot \boldsymbol{u}_{geo} \tag{3}$$

In this study, $\mathbf{u}_{geo} = (u_{geo}, v_{geo})$ is calculated based on the SSH field (Qiu et al. 2008):

$$\begin{cases} v_{geo} = \frac{g}{f} \frac{\partial SSH}{\partial x} \\ u_{geo} = -\frac{g}{f} \frac{\partial SSH}{\partial y} \end{cases}$$
 (4)

where g and f represent the gravitational acceleration and the Coriolis parameter, respectively. Similar to the terms in Eq. 2, WP in spectral space is estimated as $\widehat{\tau} \cdot \widehat{u_{qeo}}^*$.

3 Results

3.1 Performance of CRCM model

Before exploring the energetics and the potential role of wind power, it is necessary to quantify whether CRCM can capture the characteristics of the oceanic circulation system in the KOE region as observation and assimilation products. Figure 2 compares the time-mean surface SSH, EKE and wind fields during October to next March derived from FORA/ QuikSCAT (Fig. 2a) and CRCM (Fig. 2b). The patterns of mean SSH and eddy activity during the boreal winter season derived from CRCM resemble those from FORA. The Kuroshio leaves the coast of Japan around 35.5°N and forms the Kuroshio Extension jet with two quasi-standing meanders around 144°E and 150°E. To its south, a strong recirculation is presented. Compared to that of the Kuroshio Extension, the intensity of the Oyashio Extension is much weaker, as indicated by the sparse SSH isolines around 39°N-40°N. Overlying the KOE region, the northwesterly wind blowing from the Asian Continent to the Pacific Ocean with surface stress approaching 0.2 N m⁻² prevails, consistent with QuikSCAT observations. In addition to the large-scale pattern, model-simulated eddy kinetic energy (EKE) is defined as

$$EKE = \frac{1}{2} \left(ut^2 + vt^2 \right) \tag{5}$$

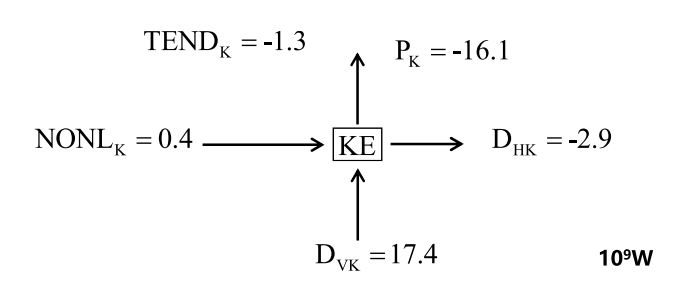


Fig. 3 Diagram for kinetic energy budget of KOE region (boxes in Fig. 2b) in upper 1000 m

where prime denotes deviation from the time-mean value, is also tested. It is noted that both mesoscale eddies and active meanders in the KOE region are involved in the EKE. In both CRCM and FORA, EKE is characterized by large values in the vicinity of the Kuroshio Extension jet with the largest amplitude located between the two crests. The maximum is found at (147°E, 35.5°N) and reaches more than 0.3 $\rm m^2~s^{-2}$. In the vertical direction, EKE is dominated by a surface-intensified structure along the Kuroshio Extension with an e-folding scale of 400 m (not shown). The consistency between the CRCM and FORA and QuikSCAT supports the validity of CRCM simulations. In the following discussion, we assess the energetics in the KOE region.

3.2 Kinetic energy balance

To find out the underlying process in regulating the kinetic energy balance, budget analysis (dashed boxes in Fig. 2b) is performed (Fig. 3). Integrated over the KOE region and upper 1000 m, the main kinetic energy source and sink are mixing and pressure work, with the contribution of tendency and nonlinearity secondary. Although the overall analysis gives us a rough picture of the EKE balance in the KOE region, it fails to capture the importance of each item in every wave number band. To get a better understanding of the dynamics, the distributions of energy terms in wavenumber-depth space are also provided (Fig. 4). It is noted that the contribution of horizontal mixing ($D_{\rm HK}$) is much smaller than that of vertical mixing ($D_{\rm VK}$; Fig. 3), thus, we treat them as one term in the following. In the KOE region, the spectrum of kinetic energy (calculated

based on $\mathcal{R}(\frac{1}{2}\widehat{u_h}\cdot\widehat{u_h}^*)$ is characterized by a peak at 2.4×10^{-5} rad m⁻¹ (about 250 km; please refer to the dashed lines in Fig. 4), close to the scale of mesoscale eddies that dominate the kinetic energy (Wang et al. 2019; Li et al. 2025). In the upper 50 m, at scales smaller than the kinetic energy peak, energy generation is dominated by generation through P_K and dissipation through nonlinear and mixing terms. This layer lies in the time-averaged mixed layer, which is significantly influenced by wind stress and surface heat flux. Additionally, it is a region characterized by active oceanic fronts and vertical motions (McWilliams 2016). Given that the model cannot resolve mixed layer instability and frontogenesis processes characteristic of submesoscale, the energy balance here can be interpreted as the turbulent thermal wind balance (Gula et al. 2014; Yang et al. 2021): Baroclinic energy stored in the horizontal buoyancy gradients associated with fronts and filaments is released through vertical mixing. This released energy is subsequently transferred to larger scales and advected away. Below 50 m, however, the energy budget is characterized by NONL_K and P_K,



87 Page 6 of 13 Ocean Dynamics (2025) 75:87

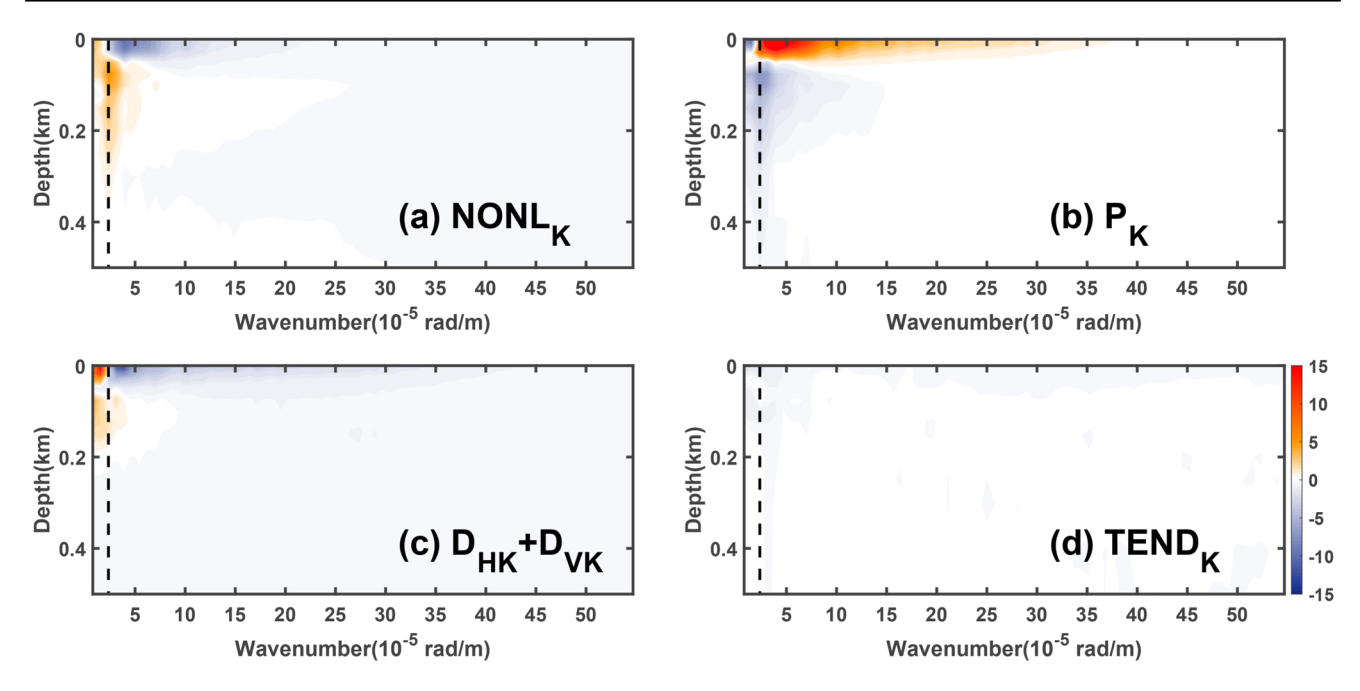


Fig. 4 Distributions of energy terms (Unit: W m $^{-1}$) in wavenumber-depth space, **a** represents NONL $_K$ term, **b** represents P_K term, **c** represents D_{HK} and D_{VK} term, **d** represents TEND $_K$ term, the dashed lines show the wavenumber with maximum kinetic energy

and the mixing term becomes much smaller. The negative P_K between 50 to 250 m is also reported by previous studies (Wang et al. 2019; Yang et al. 2021), and is associated with the downward energy flux that transports the energy generated through thermal wind balance in the upper 50 m and through baroclinic instability between 50 to 250 m into the deeper ocean. Different from the small scale, the budget of kinetic energy within scale larger than 250 km is found to be shaped by positive $D_{HK} + D_{VK}$ and $NONL_K$ terms and negative P_K . The energy balance suggests that work done by surface wind stress on the ocean, energy advected into the KOE from adjacent regions, and cross-scale energy transfer collectively sustain the horizontal pressure gradient.

In addition to the depth-integrated $NONL_K$, the integration of the $NONL_K$ term over wavenumber K is calculated to evaluate the energy cascade (Wang et al. 2019; Li et al. 2025):

$$\Pi(K) = \int_{K}^{K_{max}} NONL_K dk, \tag{6}$$

where K denotes the magnitude of the horizontal wave vector ($\sqrt{k_x^2 + k_y^2}$). The sign of NONL_K indicates local energy source (negative) or sink (positive). The integral of these contributions, $\Pi(K)$, quantifies the energy cascade. Negative (positive) $\Pi(K)$ values in wavenumber space indicate an inverse (forward) energy cascade (Scott and Wang 2005). Note that $\Pi(K)$ reliably represents the energy cascade when

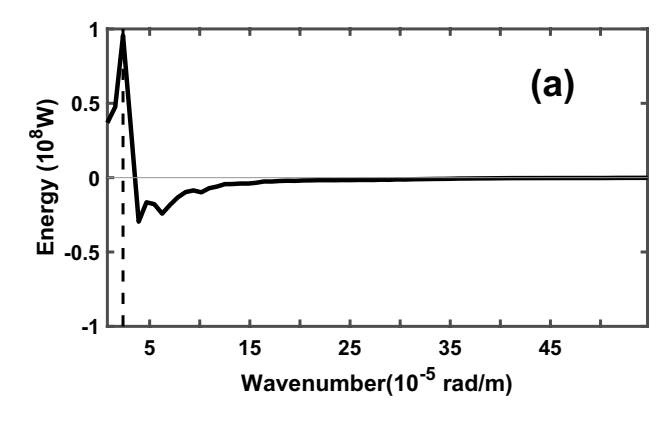
vanishing at $K_{\rm max}$ (here 60×10^{-5} rad m⁻¹, corresponding to the model's 9 km horizontal resolution), as advection processes may cause nonvanishing $\Pi(0)$. Thus, we quantify energy cascade contamination using Eq. 6 via $\frac{|\Pi(0)|}{|\Pi(K)|_{\rm max}}$, where $|\Pi(K)|_{\rm max}$ is $\Pi(K)$'s peak magnitude. Values approaching (substantially less than) 1 imply NONL_K is dominated by cross-boundary energy transport (cross-scale energy exchange). Figure 5b shows values below 0.1 in the KOE region, confirming Π as a robust energy cascade proxy.

The depth-integrated $NONL_K$ exhibits negative (positive) values at scales smaller (larger) than 4×10^{-5} rad m⁻¹, peaking near the kinetic energy maximum wavenumber (Fig. 5a), indicating upscale energy flux. Upscale trans-

fer arrest ($\frac{\partial\Pi(K)}{\partial K}=0$) initiates at NONL_K's zero-crossing (\sim 4×10⁻⁵ rad m⁻¹). The primary energy source of the inverse cascade (Π 's steepest positive slope) occurs near 4.7×10⁻⁵ rad m⁻¹, consistent with the regional Rossby deformation radius (Wang et al. 2015, 2019; Li et al. 2025). In comparison, the energy sink concentrates near the kinetic energy maximum scale. By combining the analysis of energy budget and $\Pi(K)$, it is revealed that the energy cascade's critical role—despite its small full-wavenumber-space integral—in predominantly transferring kinetic energy from scales below 4×10⁻⁵ rad m⁻¹ to scales above this threshold, thereby acting as a major large-scale kinetic energy source and significant small-scale sink.



Ocean Dynamics (2025) 75:87 Page 7 of 13 **87**



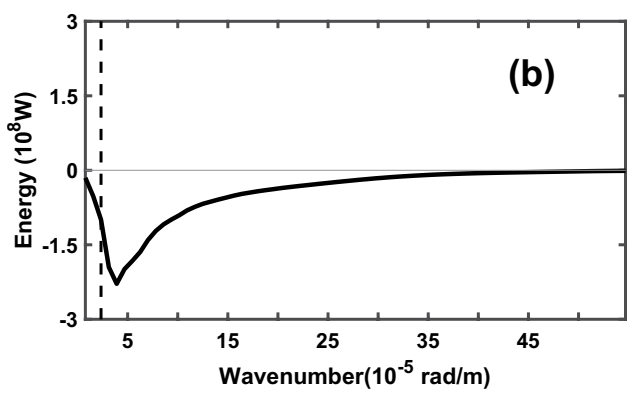


Fig. 5 (a) The depth-integrated $NONL_K$ and (b) $\Pi(K)$ in wavenumber space. The dashed lines show the wavenumber with maximum kinetic energy. The definition of $\Pi(K)$ can be found in Eq. 6

3.3 Role of wind power input

In this subsection, we first explore the characteristics of wind power and assess its role in vertical mixing. Figure 6a presents the horizontal distribution of WP derived from the CRCM model which is defined by Eq. 3, in which wind stress does overall positive work on the ocean. Significant wind power is found along the Kuroshio Extension and Oyashio Extension where the ocean current is energetic. Both the pattern and magnitude of D_{VK} integrated in the upper 1000 m highly resemble that of WP, indicating the dominating role of wind stress in shaping oceanic vertical mixing in the upper 1000 m. This is further confirmed by the spectral correlation analysis between WP and D_{VK} at each depth level (Fig. 6b). Its value in the upper 100 m is larger than 0.6 throughout horizontal wavenumbers with the maximum close to 1 at the kinetic energy maximum scale. Besides the spatial correlation, the relationship between WP and D_{VK} can also be proved by their in-phase temporal change (Fig. 6c). There is a significant linear relationship between surface energy flux WP and D_{VK}, especially near the sea surface. In the upper 20 m, the coefficient retains a value of greater than 0.8, consistent with the result based on spatial correlation shown in Fig. 6b. The correlation remains significant at 99% level up to 150 m based on the student T-test. Below 200 m, the coefficient is small. Overall, the high correlation between WP and $D_{\rm VK}$ in both spatial distribution and temporal evolution suggests a dominant role of wind stress in regulating the oceanic vertical mixing.

To further understand the characteristics of WP, we decompose it into four components as follows:

$$WP = \underbrace{\overline{\tau} \cdot \overline{u}_{geo}}_{WP_1} + \underbrace{\tau' \cdot \overline{u}_{geo}}_{WP_2} + \underbrace{\overline{\tau} \cdot u'_{geo}}_{WP_3} + \underbrace{\tau' \cdot u'_{geo}}_{WP_4}$$
(7)

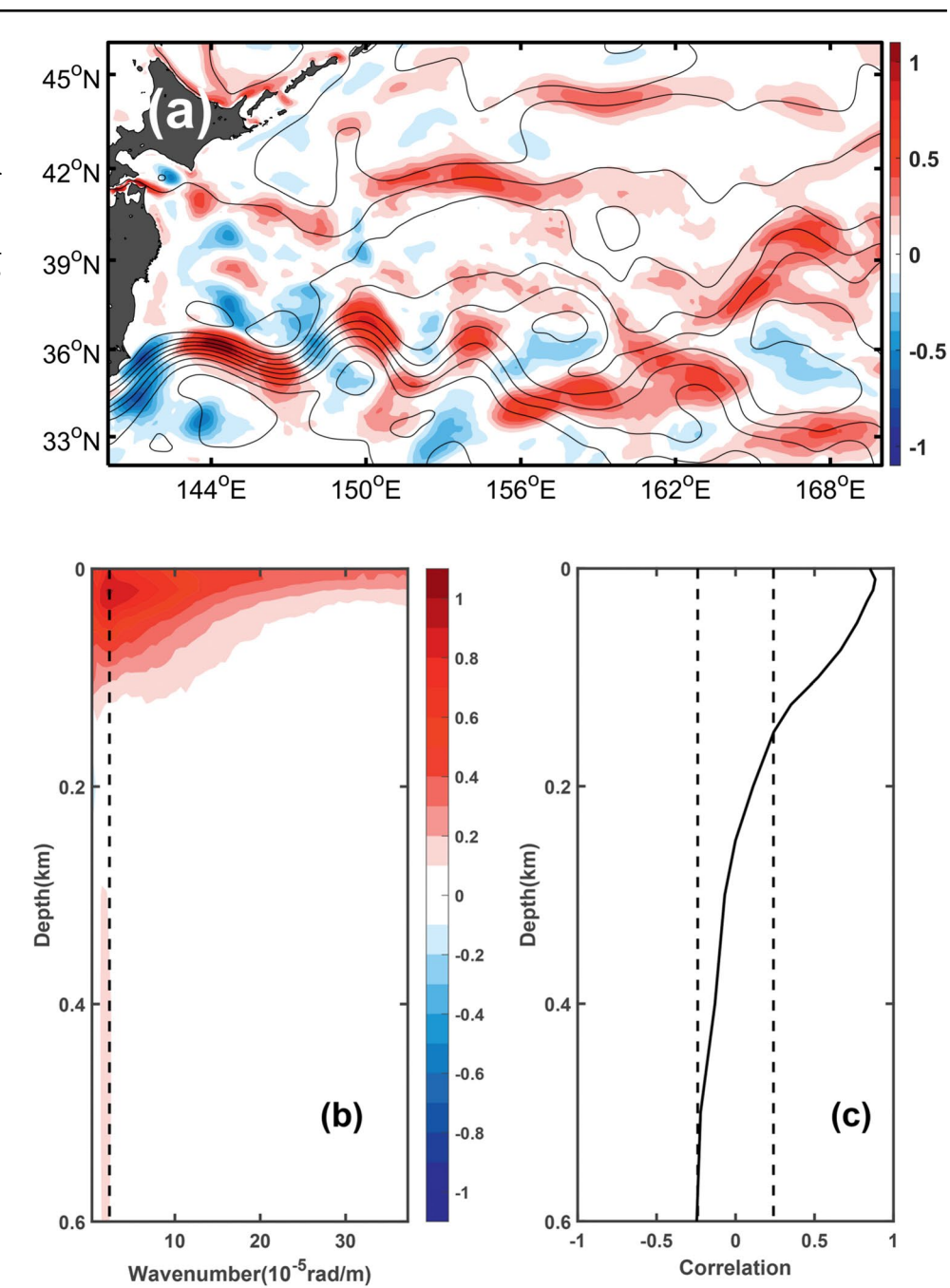
where the overbar represents the average over time. In Eq. 7, WP₁ represents work done by time-mean wind stress on time-mean circulation, WP2 work of wind stress fluctuation on time-mean circulation, WP3 work of time-mean wind stress on circulation fluctuation, and WP₄ work of wind stress fluctuation on circulation fluctuation. By breaking down WP into these components, we can disentangle how different combinations of atmospheric and oceanic variability contribute to ocean energy balance and cascade. Similar to WP, their spectral characteristics are estimated as $\widehat{\overline{\tau}} \cdot \widehat{\overline{u_{geo}}}^*$, $\widehat{\tau'} \cdot \widehat{\overline{u_{geo}}}^*$, $\widehat{\overline{\tau}} \cdot \widehat{u'_{geo}}^*$, and $\widehat{\tau'} \cdot \widehat{u'_{geo}}^*$ respectively. Figure 7 depicts the spectra of WP and its four components. Within the scale larger than 1.2×10^{-5} rad m⁻¹ (about 500 km), WP is positive and is dominated by WP₁, suggesting the driving effect of large-scale wind on the oceanic circulation. In comparison, WP is negative at the mesoscale (equal to or smaller than 2.4×10^{-5} rad m⁻¹ or 250 km) and is controlled by the WP₄, consistent with the conclusion that wind power does negative work on mesoscale eddies (Zhai et al. 2012; Yang et al. 2019, 2021; Wang et al. 2019). The time-averaged magnitude of WP₂ and WP₃ is zero over all the spectral space.

The effects of the four components on D_{VK} are estimated through the spatial and temporal correlation (Fig. 8). It is revealed that wind power input to the time-mean circulation (WP₁ and WP₂, Fig. 8a and b) mainly affects D_{VK} at the large scale (>500 km) in the upper 150 m. Figure 9 further depicts that the temporal variability of wavenumber-integrated D_{VK} is mainly caused by WP₂. Differently, the correlation of wind power input to the circulation fluctuation (WP3 and WP₄, Fig. 8c and d) and D_{VK} is high at the mesoscale in space, though their impact in regulating the time variation of D_{VK} is overshadowed by WP₂ (Fig. 9). Compared to that in Fig. 8c, the pattern of correlation in Fig. 8d is closer to Fig. 6b, suggesting a closer relationship of WP₄ in regulating D_{VK} at the mesoscale and smaller scale than WP₃. In addition to this effect at the mesoscale, it is also noted that WP₃ depicts significant consistency with D_{VK} at the scale larger than 500 km in the subsurface (200—600 m), which may be due to the compatibility between the time-averaged



87 Page 8 of 13 Ocean Dynamics (2025) 75:87

Fig. 6 (a) Horizontal distribution of WP (shading; Unit: 0.1 W m⁻²) and SSH (contours; Unit: m) derived from CRCM model. b Correlation coefficient between WP and D_{VK} in depth-wavenumber space, the dashed line shows the wavenumber with maximum kinetic energy. c Correlation coefficient between the timeseries of WP and D_{VK} , the dashed lines denote the confidence interval based on 99% student T-test



wind field and the large-scale circulation. To summarize, the surface wind injects energy into the ocean and controls its fluctuation at the large scale, whereas it draws energy from the ocean at the mesoscale.

Besides controlling D_{VK} , WP_3 and WP_4 may also affect the oceanic energy cascade indirectly, given that they contribute to oceanic kinetic energy dissipation at the scale corresponding to the source for the inverse energy cascade—the Rossby deformation radius (Fig. 5b). To confirm this relationship, spatial correlation between $NONL_K$ at each depth and WP_3/WP_4 is calculated (Fig. 10). In the

upper 100 m, WP₃ shows an in-phase distribution with NONL_K (Fig. 10a), though the correlation coefficient is not large (-0.25, significant at 90% confidence level). In addition, we also calculate the temporal correlation between WP₃ and the minimum of $\Pi(K)$ (corresponds to $\frac{\partial \Pi(K)}{\partial K} = 0$ at around 4.7×10^{-5} rad m⁻¹ and denotes the magnitude of inverse cascade; Fig. 5b; Wang et al. 2015), and find that the magnitude of correlation reaches 0.4 (significant at 90% confidence level). The two significant correlations indicate that the work of time-mean wind stress on circulation fluctuations affects cross-scale interactions through



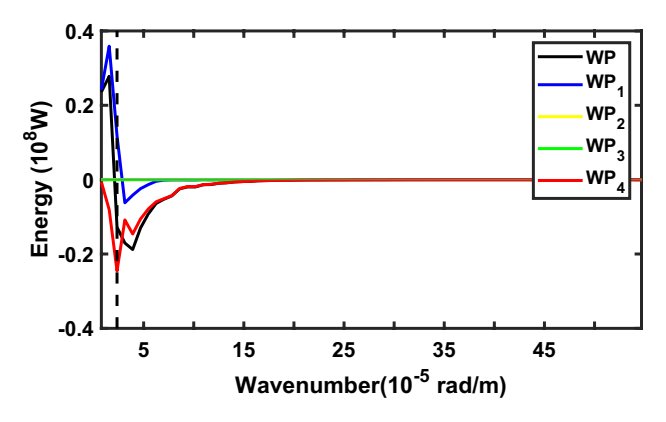


Fig. 7 The spectra of WP (Black) and its four components, where WP $_{\rm l}$ -WP $_{\rm 4}$ are represented by the blue line, yellow line, green line and red line, respectively. The dashed line denotes the wavenumber with maximum kinetic energy. It is noted that the green line completely covers the yellow line because the time-mean values of WP2 and WP3 are both zero

altered mixing processes, thereby modulating mesoscale energy levels. However, their small magnitude, as well as the different correlation patterns in Figs. 8c and 10a, indicate that WP_3 does not dominate the effect on the energy cascade, which is also regulated by other oceanic processes. Different from WP_3 , the role of WP_4 in regulating $NONL_K$ is insignificant (Fig. 10b), implying that the effect of work done by time-varying wind on eddies is locally in spectral space and is secondary in affecting the energy cascade.

4 Conclusion

Based on the daily mean output of high-resolution CRCM simulation, the kinetic energy balance in wave number space in the KOE region and the role of wind power are explored. The major results of this study are summarized as follows:

- The kinetic energy balance in the KOE region is characterized by the quasi-balance between vertical mixing and pressure work, with the contribution of the nonlinear effect and horizontal mixing negligible.
- 2. An upscale energy flux is detected from a large wavenumber to $2.4 \times 10-5$ rad m-1 (about 250 km), where the spectrum of kinetic energy presents a peak.
- 3. Wind power is found to inject energy into the ocean and control its fluctuation at the large scale, whereas it draws energy from the ocean and regulates the inverse energy cascade at the mesoscale.

This study explores the oceanic kinetic energy balance and the role of wind power in the KOE region. Together with an early work (Li et al. 2025), we provide a picture of how and to what extent the mesoscale air-sea interaction could affect the oceanic kinetic energy. A better understanding of associated dynamics will be a forward step to the better understanding of cross-scale interaction of ocean processes in the vicinity of intense midlatitude oceanic jet regions, as well as

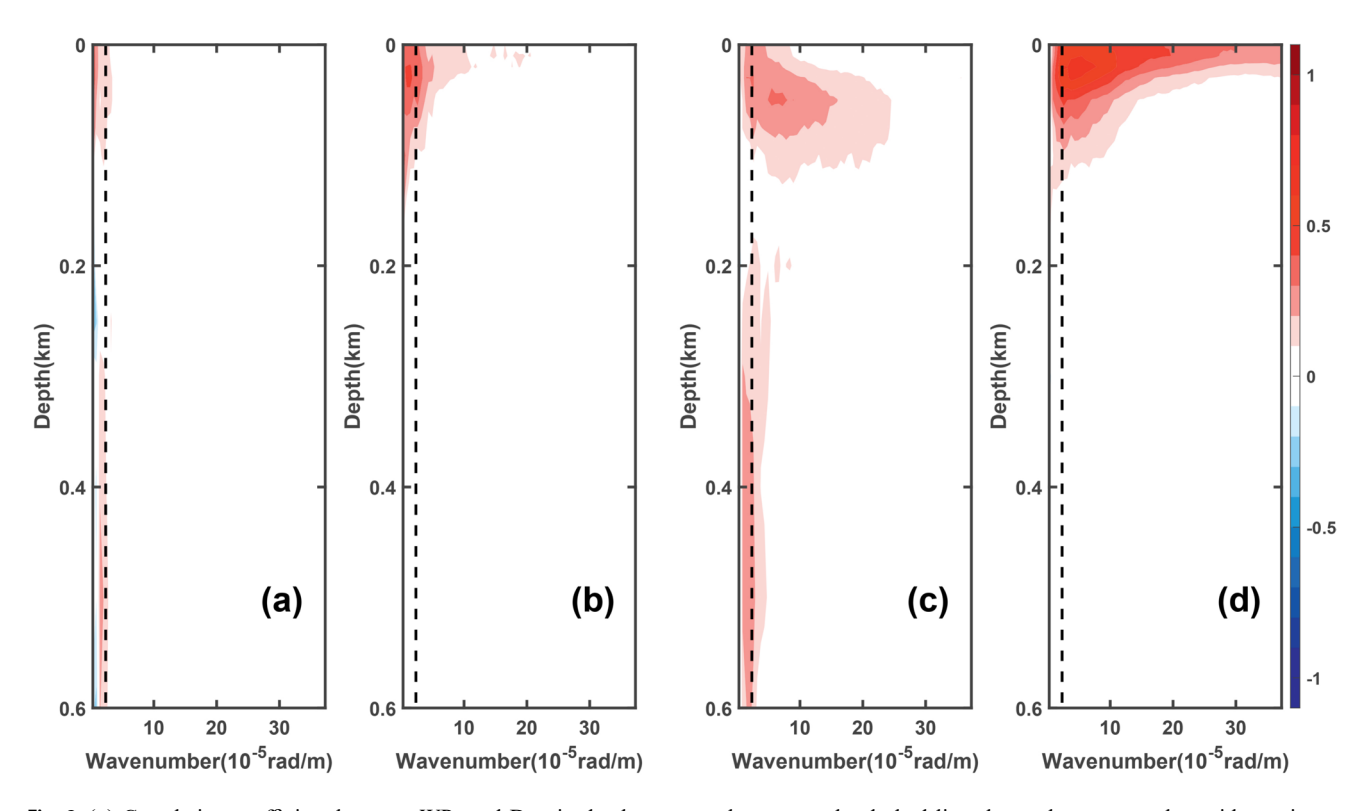


Fig. 8 (a) Correlation coefficient between WP_1 and D_{VK} in depth-wavenumber space, the dashed line shows the wavenumber with maximum kinetic energy. **b-d** are similar to (a), but with WP_1 replaced by WP_2 , WP_3 , WP_4 respectively



87 Page 10 of 13 Ocean Dynamics (2025) 75:87

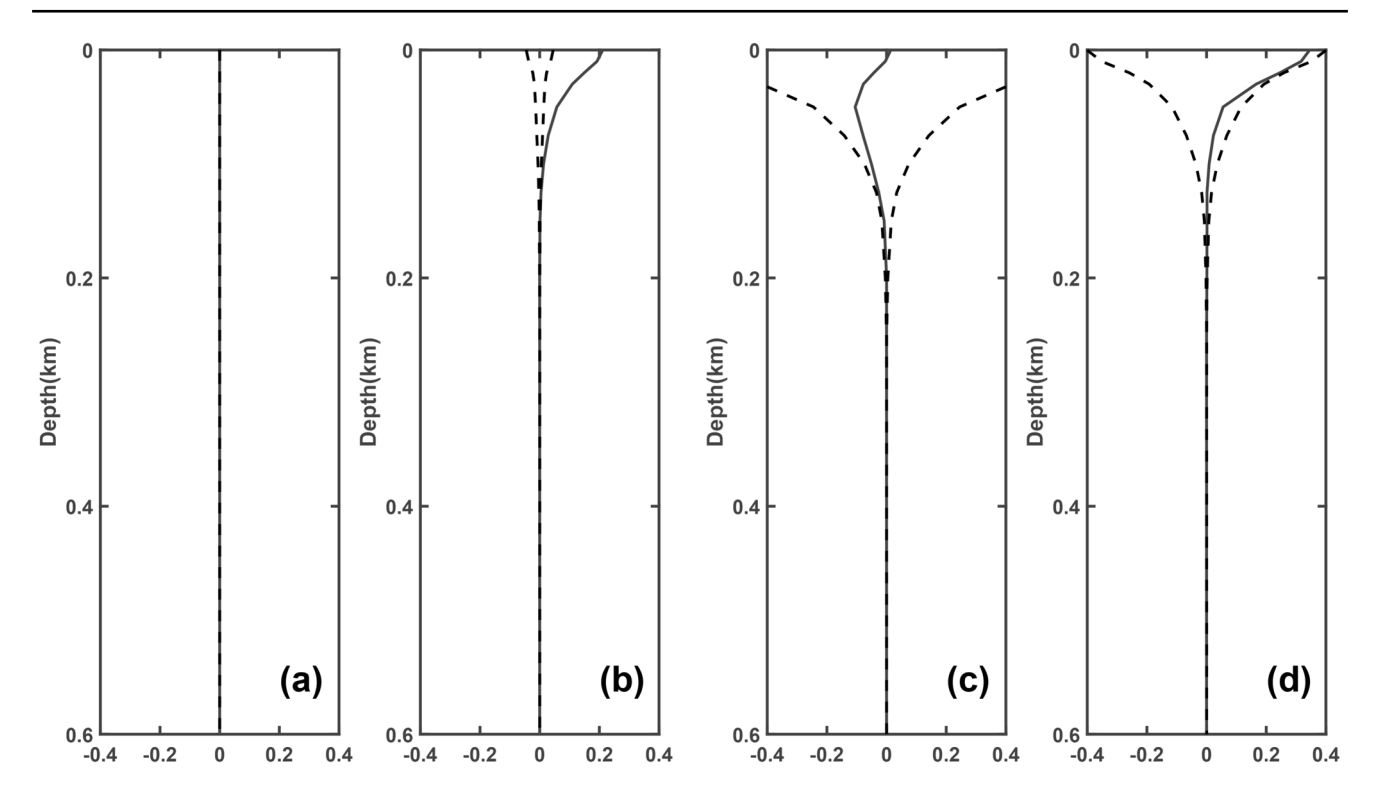


Fig. 9 Regression coefficient by regressing D_{VK} upon (a) WP_1 , b WP_2 , c WP_3 and (d) WP_4 . Dash lines indicates rejection region at 90% confidence level based on T-test

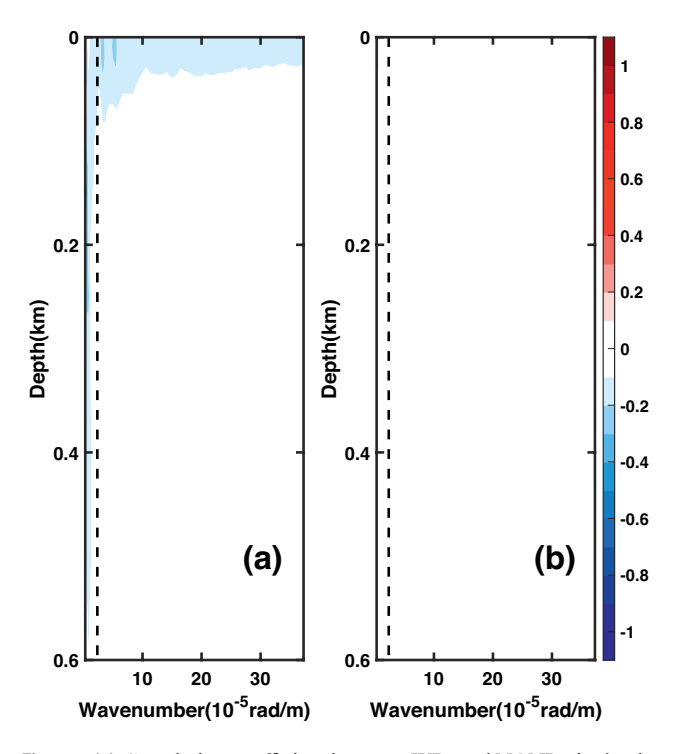


Fig. 10 (a) Correlation coefficient between WP $_3$ and NONL $_K$ in depthwavenumber space, the dashed line shows the wavenumber with maximum kinetic energy. **b** is similar to (a) but shows the correlation coefficient between WP $_4$ and NONL $_K$

the development of improved parameterizations of air-sea interactions for climate model simulation (e.g. Chen et al. 2024; Huang et al. 2024; Qiu 2023). In addition, it should be noted that the CRCM used in this study is mesoscale-resolving, which cannot resolve the oceanic submesoscale processes that are proven to be important in oceanic kinetic energy balance (McWilliams 2016; Su et al. 2018) and climate system (Sullivan et al. 2020; Yang et al. 2024; Shao and Wu 2024; Vivant et al. 2025). Next, how the submeso-scale air-sea interaction modulates oceanic energy balance needs to be investigated based on submesoscale-resolving simulations.

Acknowledgements Computation for this work is supported by the Marine Big Data Center of Institute for Advanced Ocean Study of Ocean University of China and Laoshan Laboratory. We sincerely thank the two anonymous reviewers and Editor Nagano for their suggestions and assistance in revising this paper.

Author contributions H. Y. wrote the main manuscript text with contributions of M. L. and J. C.; M. L. conduct the CRCM model and analyze the data; H. Y. is grantee of Natural Science Foundation of China and supervised the work; all authors edited and reviewed the manuscript.

Funding This research is supported by Natural Science Foundation of China (42422601, 42176006 and 42225601).



Data availability Four-dimensional variational Ocean Re-Analysis for the Western North Pacific over 30 years (FORA-WNP30) product is available at https://synthesis.jamstec.go.jp/FORA/e/ (Usui et al., 2017). The wind stress data provided by SeaWinds scatterometer on the QuikSCAT satellite are available at https://data.remss.com/qscat/qscat_wind_vectors_v04/. The CRCM model output is available by contacting M. L. (mkli@ouc.edu.cn).

Declarations

Ethical approval Not applicable.

Competing interests The authors declare no competing interests.

References

- Aluie H, Hecht M, Vallis G (2018) Mapping the energy cascade in the North Atlantic Ocean: the coarse-graining approach. J Phys Oceanogr 48(2):225–244
- Arbic BK, Flierl GR (2004) Effects of mean flow direction on energy, isotropy, and coherence of baroclinically unstable beta-plane geostrophic turbulence. J Phys Oceanogr 34(1):77–93
- Boccaletti G, Ferrari R, Fox-Kemper B (2007) Mixed layer instabilities and restratification. J Phys Oceanogr 37:2228–2250
- Cai J, Li M, Yang H, Chen Z (2024) Role of air-sea interaction in the energy balance of anticyclonic and cyclonic eddies in the Kuroshio Extension. J Geophys Res Oceans 129(4):e2023JC020682
- Chelton DB, Esbensen SK, Schlax MG et al (2001) Observations of coupling between surface wind stress and sea surface temperature in the eastern tropical Pacific. J Climate 14(7):1479–1498
- Chelton DB, Schlax MG, Freilich MH, Milliff RF (2004) Satellite measurements reveal persistent small-scale features in ocean winds. Science 303(5660):978–983
- Chelton DB, Schlax MG, Samelson RM (2011) Global observations of nonlinear mesoscale eddies. Prog Oceanogr 91(2):167–216
- Chen R, Flierl GR, Wunsch C (2014) A description of local and nonlocal eddy-mean flow interaction in a global eddy-permitting state estimate. J Phys Oceanogr 44(9):2336–2352
- Chen R, Flierl GR, Wunsch C (2015) Quantifying and interpreting striations in a subtropical gyre: a spectral perspective. J Phys Oceanogr 45(2):387–406
- Chen R, Thompson AF, Flierl GR (2016) Time-dependent eddy-mean energy diagrams and their application to the ocean. J Phys Oceanogr 46(9):2827–2850
- Chen G, Han W, Huang RX, Wang D (2024) Equatorial waves substantially modulate currents in the tropical Indian Ocean. Innov Geosci 2(1):100053
- Chou MD, Suarez MJ (1994) An efficient thermal infrared radiation parameterization for use in general circulation models. NASA Tech Memo 104606
- Dauhajre DP, McWilliams JC (2018) Diurnal evolution of submesoscale front and filament circulations. J Phys Oceanogr 48:2343–2361
- Dong C, Dong J, Zhang H, Yang J (2022) Submesoscale processesinduced vertical heat transport modulated by oceanic mesoscale eddies. Deep-Sea Res Pt II 202:105138
- Eden C, Dietze H (2009) Effects of mesoscale eddy/wind interactions on biological new production and eddy kinetic energy. J Geophys Res 114(C5):C05023
- Fox-Kemper B, Ferrari R, Hallberg R (2008) Parameterization of mixed layer eddies. Part I: theory and diagnosis. J Phys Oceanogr 38:1145–1165

- Gaube P, Chelton DB, Samelson RM, Schlax MG, O'Neill LW (2015) Satellite observations of mesoscale eddy-induced Ekman pumping. J Phys Oceanogr 45(1):104–132
- Griffies SM, Hallberg RW (2000) Biharmonic friction with a Smagorinsky-like viscosity for use in large-scale eddy-permitting ocean models. Mon Weather Rev 128(8):2935–2946
- Gula J, Molemaker MJ, McWilliams JC (2014) Submesoscale cold filaments in the Gulf Stream. J Phys Oceanogr 44:2617–2643
- Guo Y, Bishop SP (2022) Surface divergent eddy heat fluxes and their impacts on mixed layer eddy-mean flow interactions. J Adv Model Earth Syst 14(4):e2021MS002863
- Guo Y, Bishop S, Bryan F, Bachman S (2022) A global diagnosis of eddy potential energy budget in an eddy-permitting ocean model. J Phys Oceanogr 52(8):1731–1748
- Hogg A, Dewar WK, Berloff P et al (2009) The effects of mesoscale ocean-atmosphere coupling on the large-scale ocean circulation. J Climate 22(15):4066–4082
- Hong SY, Pan HL (1996) Nonlocal boundary layer vertical diffusion in a medium-range forecast model. Mon Weather Rev 124:2322–2339
- Hoskins BJ, Valdes PJ (1990) On the existence of storm-tracks. J Atmos Sci 47(15):1854–1864
- Hu D, Wu L, Cai W et al (2015) Pacific Western Boundary Currents and their roles in climate. Nature 522(7556):299-308
- Huang P, Zheng X, Li X, Hu K, Zhou Z (2024) More complex interactions: continuing progress in understanding the dynamics of regional climate change under a warming climate. Innovation 4(2):100398
- Hurlburt HE, Wallcraft AJ, Schmitz J, Hogan PJ, Metzger EJ (1996) Dynamics of the Kuroshio/Oyashio current system using eddyresolving models of the North Pacific Ocean. J Geophys Res: Oceans 101(C1):941–976
- Jayne SR, Hogg NG, Waterman SN et al (2009) The Kuroshio Extension and its recirculation gyres. Deep Sea Res Part I 56(12):2088–2099
- Ji J, Dong C, Zhang B et al (2018) Oceanic eddy characteristics and generation mechanisms in the Kuroshio Extension region. J Geophys Res Oceans 123(11):8548–8567
- Jing Z, Chang P, Shan X, Wang S, Wu L, Kurian J (2019) Mesoscale SST dynamics in the Kuroshio-Oyashio extension region. J Phys Oceanogr 49(5):1339–1352
- Kain JS (2004) The Kain-fritsch convective parameterization: an update. J Appl Meteorol 43(1):170–181
- Kaspi Y, Schneider T (2013) The role of stationary eddies in shaping midlatitude storm tracks. J Atmos Sci 70(8):2596–2613
- Kelly KA, Small RJ, Samelson RM et al (2010) Western boundary currents and frontal air–sea interaction: Gulf Stream and Kuroshio Extension. J Climate 23(21):5644–5667
- Kida S, Mitsudera H, Aoki S et al (2016) Oceanic fronts and jets around Japan: a review. In: "Hot Spots" in the climate system: new developments in the extratropical ocean-atmosphere interaction research pp 1–30
- Kobayashi S, Ota Y, Harada Y et al (2015) The JRA-55 reanalysis: general specifications and basic characteristics. J Meteorol Soc JPN Ser II 93(1):5–48
- Large WG, McWilliams JC, Doney SC (1994) Oceanic vertical mixing: a review and a model with a nonlocal boundary layer parameterization. Rev Geophys 32(4):363–403
- Li M, Cai J, Yang H, Chen Z, Wu L (2025) Oceanic eddy kinetic energy in the spectral space regulated by mesoscale air-sea heat exchange in the Kuroshio Extension. Adv Atmos Sci in press. htt ps://doi.org/10.1007/s00376-024-4353-x
- Lin YL, Farley RD, Orville HD (1983) Bulk parameterization of the snow field in a cloud model. J Climate Appl Meteorol 22:1065–1092



87 Page 12 of 13 Ocean Dynamics (2025) 75:87

Liu H, Li W, Chen S, Fang R, Li Z (2018) Atmospheric response to mesoscale ocean eddies over the South China Sea. Adv Atmos Sci 35(9):1189–1204

- Long Y, Zhu X, Guo X et al (2021) Variations of the Kuroshio in the Luzon Strait revealed by EOF analysis of repeated XBT data and sea-level anomalies. J Geophys Res Oceans 126:e2020JC016849
- Ma X, Jing Z, Chang P, Liu X, Montuoro R, Small RJ et al (2016) Western boundary currents regulated by interaction between ocean eddies and the atmosphere. Nature 535(7613):533–537
- McWilliams JC (2016) Submesoscale currents in the ocean. Proc Royal Soc A: Math Phys Eng Sci 472(2189):20160117
- McWilliams JC, Gula J, Molemaker MJ (2019) The Gulf Stream North Wall: ageostrophic circulation and frontogenesis. J Phys Oceanogr 49:893–916
- Mlawer EJ, Taubman SJ, Brown PD, Iacono MJ, Clough SA (1997) Radiative transfer for inhomogeneous atmosphere: RRTM, a validated correlated-k model for the longwave. J Geophys Res 102(D14):16663–16682
- Nakamura M, Miyama T (2014) Impacts of the Oyashio temperature front on the regional climate. J Climate 27(20):7861–7873
- Nakamura H, Shimpo A (2004) Seasonal variations in the southern hemisphere storm tracks and jet streams as revealed in a reanalysis dataset. J Climate 17:1828–1844
- Nakayama M, Nakamura H, Ogawa F (2021) Impacts of a midlatitude oceanic frontal zone for the baroclinic annular mode in the Southern Hemisphere. J Climate 34(18):7389–7408
- Nishikawa H, Nishikawa S, Ishizaki H, Wakamatsu T, Ishikawa Y (2020) Detection of the Oyashio and Kuroshio fronts under the projected climate change in the 21st century. Prog Earth Planet Sci 7:1–12
- Noh Y, Kim HJ (1999) Simulations of temperature and turbulence structure of the oceanic boundary layer with the improved nearsurface process. J Geophys Res Oceans 104(C7):15621–15634
- Nonaka M, Nakamura H, Taguchi B et al (2009) Air–sea heat exchanges characteristic of a prominent midlatitude oceanic front in the South Indian Ocean as simulated in a high-resolution coupled GCM. J Climate 22(24):6515–6535
- Qiu B (2019) Kuroshio and Oyashio currents. Encyclopedia of Ocean Sci 3:384–394
- Qiu B (2023) Observational and theoretical studies of the North Pacific upper ocean circulation and its variability. Oceanogr JPN 32:67–93
- Qiu B, Chen S (2005) Variability of the Kuroshio Extension jet, recirculation gyre, and mesoscale eddies on decadal time scales. J Phys Oceanogr 35(11):2090–2103
- Qiu B, Chen S (2010) Eddy-mean flow interaction in the decadally modulating Kuroshio Extension system. Deep-Sea Res Pt II 57(13–14):1098–1110
- Qiu B, Kelly KA, Joyce TM (1991) Mean flow and variability in the Kuroshio Extension from Geosat altimetry data. J Geophys Res Oceans 96(C10):18491–18507
- Qiu B, Scott R, Chen S (2008) Length scales of eddy generation and nonlinear evolution of the seasonally-modulated South Pacific Subtropical Countercurrent. J Phys Oceanogr 38(7):193–206
- Qiu B, Nakano T, Chen S, Klein P (2022) Bi-directional energy cascades in the Pacific Ocean from equator to subarctic gyre. Geophys Res Lett 49(8):e2022GL097713
- Qu T, Mitsudera H, Qiu B (2001) A climatological view of the Kuroshio/ Oyashio system east of Japan. J Phys Oceanogr 31(9):2575–2589
- Renault L, McWilliams JC, Masson S (2017) Satellite observations of imprint of oceanic current on wind stress by air-sea coupling. Sci Rep 7(1):17747
- Renault L, Lemarié F, Arsouze T (2019) On the implementation and consequences of the oceanic currents feedback in ocean—atmosphere coupled models. Ocean Model 141:101423

- Renault L, Masson S, Oerder V, Colas F, McWilliams JC (2023) Modulation of the oceanic mesoscale activity by the mesoscale thermal feedback to the atmosphere. J Phys Oceanogr 53(7):1651–1667
- Rhines P, Hakkinen S, Josey SA (2008) Is oceanic heat transport significant in the climate system? In Arctic–Subarctic Ocean Fluxes. Springer, pp 87–109
- Scharffenberg MG, Stammer D (2010) Seasonal variations of the largescale geostrophic flow field and eddy kinetic energy inferred from the TOPEX/Poseidon and Jason-1 tandem mission data. J Geophys Res Oceans 115(C2):C02008
- Schlösser F, Eden C (2007) Diagnosing the energy cascade in a model of the North Atlantic. Geophys Res Lett 34(2):L02604
- Scott R, Wang F (2005) Direct evidence of an oceanic inverse kinetic energy cascade from satellite altimetry. J Phys Oceanogr 45(9):1650–1666
- Seo H (2017) Distinct influence of air—sea interactions mediated by mesoscale sea surface temperature and surface current in the Arabian Sea. J Climate 30(20):8061–8080
- Seo H, Miller AJ, Norris JR (2015) Eddy-wind interaction in the California current system: dynamics and impacts. J Phys Oceanogr 46:439–459
- Seo H, O'Neill LW, Bourassa MA et al (2023) Ocean mesoscale and frontal-scale ocean–atmosphere interactions and influence on large-scale climate: a review. J Climate 36(7):1981–2013
- Shan X, Jing Z, Gan B, Wu L, Chang P, Ma X et al (2020) Surface heat flux induced by mesoscale eddies cools the Kuroshio-Oyashio Extension region. Geophys Res Lett 47(1):e2019GL086050
- Shao M, Wu L (2024) Atmospheric fronts shaping the (Sub) mesoscale SST-wind coupling over the Southern Ocean: observational case. J Geophys Res Atmos 129(8):e2023JD039386
- Siegelman L, Klein P, Rivière P, Thompson AF, Torres HS, Flexas M, Menemenlis D (2020) Enhanced upward heat transport at deep submesoscale ocean fronts. Nat Geosci 13(1):50–55
- Skamarock WC, Klemp JB, Dudhia J et al (2008) A description of the advanced research WRF version 3. NCAR Tech Note 475(125):10-5065
- Smagorinsky J (1963) General circulation experiments with the primitive equations: I. The Basic Experiment Month Weather Rev 91(3):99–164
- Small R, Szoeke D, Xie SP et al (2008) Air–sea interaction over ocean fronts and eddies. Dyn Atmos Oceans 45(3–4):274–319
- Sprintall J, Roemmich D, Stanton B, Bailey R (1995) Regional climate variability and Ocean heat transport in the southwest Pacific Ocean. J Geophys Res 100:15865–15871
- Stommel H (1979) Oceanic warming of western Europe. P Natl Acad Sci USA 76:2518–2521
- Su Z, Wang J, Klein P, Thompson A, Menemenlis D (2018) Ocean submesoscales as a key component of the global heat budget. Nat Commun 9(1):775
- Sullivan PP, McWilliams JC, Weil JC, Patton EG, Fernando HJ (2020) Marine boundary layers above heterogeneous SST: across-front winds. J Atmos Sci 77(12):4251–4275
- Taylor JR, Thompson AF (2023) Submesoscale dynamics in the upper ocean. Annu Rev Fluid Mech 55:103–127
- Thomas LN, Taylor JR, Ferrari R, Joyce TM (2013) Symmetric instability in the Gulf Stream. Deep Sea Res Part II 91:96–110
- Tsujino H, Usui N, Nakano H (2006) Dynamics of Kuroshio path variations in a high-resolution general circulation model. J Geophys Res Oceans 111(C11):C11001
- Usui N, Wakamatsu T, Tanaka Y et al (2017) Four-dimensional variational ocean reanalysis: a 30-year high-resolution dataset in the western North Pacific (FORA-WNP30). J Oceanogr 73:205–233
- Vivant F, Siegelman L, Klein P, Torres HS, Menemenlis D, Molod AM (2025) Ocean submesoscale fronts induce diabatic heating and convective precipitation within storms. Commun Earth Environ 6(1):69



Wang Q, Pierini S (2020) On the role of the Kuroshio Extension bimodality in modulating the surface eddy kinetic energy seasonal variability. Geophys Res Lett 47(3):e2019GL086308

- Wang S, Liu Z, Pang C (2015) Geographical distribution and anisotropy of the inverse kinetic energy cascade, and its role in the eddy equilibrium processes. J Geophys Res Oceans 120(7):4891–4906
- Wang S, Jing Z, Zhang Q, Chang P, Chen Z, Liu H, Wu L (2019) Ocean eddy energetics in the spectral space as revealed by high-resolution general circulation models. J Phys Oceanogr 49(11):2815–2827
- Wang S, Jing Z, Wu L et al (2022) El niño/Southern oscillation inhibited by submesoscale ocean eddies. Nat Geosci 15(2):112–117
- Waterman S, Hogg NG, Jayne SR (2011) Eddy-mean flow interaction in the Kuroshio Extension region. J Phys Oceanogr 41(6):1182–1208
- Wu B, Lin X, Qiu B (2018) Meridional shift of the Oyashio Extension front in the past 36 years. Geophys Res Lett 45(17):9042–9048
- Wu B, Lin X, Qiu B (2019) On the seasonal variability of the Oyashio Extension fronts. Clim Dyn 53:7011–7025
- Xie SP (2004) Satellite observations of cool ocean-atmosphere interaction. Bull Amer Meteorol Soc 85(2):195-208
- Yang Y, Liang XS, Qiu B, Chen S (2017) On the decadal variability of the eddy kinetic energy in the Kuroshio Extension. J Phys Oceanogr 47(5):1169–1187
- Yang H, Qiu B, Chang P, Wu L, Wang S, Chen Z, Yang Y (2018) Decadal variability of eddy characteristics and energetics in the Kuroshio Extension: unstable versus stable states. J Geophys Res Oceans 123(9):6653–6669
- Yang H, Chang P, Qiu B, Zhang Q, Wu L, Chen Z, Wang H (2019) Mesoscale air–sea interaction and its role in eddy energy dissipation in the Kuroshio Extension. J Climate 32(24):8659–8676

- Yang H, Wu L, Chang P, Qiu B, Jing Z, Zhang Q, Chen Z (2021) Mesoscale energy balance and air—sea interaction in the Kuroshio Extension: low-frequency versus high-frequency variability. J Phys Oceanogr 51(3):895–910
- Yang C, Yang H, Chen Z, Gan B, Liu Y, Wu L (2023) Seasonal variability of eddy characteristics and energetics in the Kuroshio Extension. Ocean Dyn 73(8):531–544
- Yang H, Chen Z, Sun S et al (2024) Observations reveal intense airsea exchanges over submesoscale ocean front. Geophys Res Lett 51(2):e2023GL106840
- Yasuda I (2003) Hydrographic structure and variability in the Kuroshio-Oyashio transition area. J Oceanogr 59:389–402
- Zhai X, Johnson HL, Marshall D, Wunsch C (2012) On the wind power input to the ocean general circulation. J Phys Oceanogr 42(8):1357–1365
- Zhou G, Cheng X (2022) Impacts of oceanic fronts and eddies in the Kuroshio-Oyashio Extension region on the atmospheric general circulation and storm track. Adv Atmos Sci 39(1):22–54
- Zhu R, Yang H, Li M, Chen Z, Ma X, Cai J, Wu L (2024) Observations reveal vertical transport induced by submesoscale front. Sci Rep 14(1):4407

Publisher's Note Springer Nature remains neutral with regard to jurisdictional claims in published maps and institutional affiliations.

Springer Nature or its licensor (e.g. a society or other partner) holds exclusive rights to this article under a publishing agreement with the author(s) or other rightsholder(s); author self-archiving of the accepted manuscript version of this article is solely governed by the terms of such publishing agreement and applicable law.

